Biomaterials Science

ROYAL SOCIETY OF CHEMISTRY

PAPER

View Article Online
View Journal | View Issue

Cite this: *Biomater. Sci.*, 2025, **13**, 1286

3D bioprinted poly(lactic acid) scaffolds infused with curcumin-loaded nanostructured lipid carriers: a promising approach for skin regeneration

Renuka Vijayaraghavan,[a,b] M. Vidyavathi,*[c] R. V. Suresh Kumar,[d] Sravanthi Loganathan *[a,b] and Ravi Babu Valapa *[a,b]

Nanotechnology and 3D bioprinted scaffolds are revolutionizing the field of wound healing and skin regeneration. By facilitating proper cellular movement and providing a customizable structure that replicates the extracellular matrix, such technologies not only expedite the healing process but also ensure the seamless integration of new skin layers, enhancing tissue repair and promoting overall cell growth. This study centres on the creation and assessment of a nanostructured lipid carrier containing curcumin (CNLC), which is integrated into a 3D bioprinted PLA scaffold system. The goal is to investigate its potential as a vehicle for delivering poorly soluble curcumin for enhanced wound healing. The developed CNLC exhibited an oval morphology and average particle size of 292 nm. The entrapment efficiency (EE) was 81.37 ± 0.85%, and the drug loading capacity was 6.59 ± 1.61%. CNLC was then integrated into PLA-based 3D bioprinted scaffolds, and physicochemical analyses were conducted to evaluate their properties. Cell viability studies carried out using fibroblast cells demonstrated that the PLA/CNLC scaffolds are non-cytotoxic. *In vivo* experiments showed that the PLA/CNLC scaffolds exhibited complete wound contraction and closure of full-thickness wounds within a period of 21 days. The findings confirmed the scaffold's capacity as a tool for accelerating wound healing. The research emphasises the need for using biomimetic 3D printed scaffold materials and the promise of nanobiotechnology in enhancing treatment efficacy.

Received 20th November 2024,
Accepted 4th January 2025

DOI: 10.1039/d4bm01550a

rsc.li/biomaterials-science

1. Introduction

Human skin extends to a surface area of around 20 square feet and accounts for 15% of the total body weight of a person.[1] It prevents damage to the internal parts due to environmental factors such as temperature, humidity, pressure, and chemicals. It helps with temperature control, immune system monitoring, preventing water loss, sensitivity, and agglutinating vitamin D3.[2–4] A wound is any disruption to the normally occurring cellular structure of skin. The classification of wound depends on its genesis, depth, location, damage type, and outward appearance.[5] In the medical field, wounds may be either chronic or acute. While acute wounds often heal on their own within a few weeks, chronic wounds may take much longer to heal owing to persistent inflammation. Chronic wounds are exacerbated by trauma, obesity, age, and persistent diseases like diabetes and cancer.[6,7] The complex physiological process of wound healing involves overlapping stages of homeostasis, inflammation, proliferation, and tissue remodelling that are carefully coordinated with each other.[8] Fibroblasts, fibrinopeptides, macrophages, interleukin-8 (IL-8), keratinocytes, platelets, and many other biochemical messengers accumulate in injured regions, setting off a chain reaction of complicated biological and chemical processes that aid in the repair of damaged tissues. Poor and faulty healing of wounded tissues may result from any interference with this normal wound recovery process, such as sepsis, fissure, anoxia, or immune dysregulation.[9–12] Several conditions, both inherited and acquired, such as diabetes, interfere with the body's natural ability to heal wounds. Higher inflammation and aberrant cellular infiltration, defective cytokine generation, neuritis, and insufficient neo-angiogenesis define chronic wounds. A growing older population, rising health care costs, and the ongoing risk of diabetes and obesity

[a]*Electrochemical Process Engineering, CSIR-Central Electrochemical Research Institute (CECRI), Karaikudi-630003, Tamil Nadu, India.*
E-mail: lsravanthi@cecri.res.in, lsravanthicecri@gmail.com, vravibabu@cecri.res.in, vravibabucecri@gmail.com
[b]*Academy of Scientific and Innovative Research (AcSIR), Ghaziabad-201002, India*
[c]*Institute of Pharmaceutical Technology, Sri Padmavati Mahila Visvavidyalayam, Tirupati, Andhra Pradesh, 517502, India*
[d]*Department of Surgery and Radiology, SV Veterinary University, Tirupati, Andhra Pradesh, 517502, India*

around the world make them a major clinical and socioeconomic concern.[13]

This suggests that there is a great need and opportunity for further study of wound healing. The inherent promotion of natural healing processes involved in plants has made them a focal point of research and study in this field.[14] With the development of science, attention has switched from plants as a whole to their active chemical components. In terms of promoting wound healing, curcumin ranks first. Curcumin, found in the rhizome of both *Curcuma longa* and *Curcuma aromatica*, is a low-molecular-weight polyphenolic component.[15] There are many bioactive compounds found in turmeric rhizomes, but the most abundant is curcumin (77%), followed by demethoxycurcumin (17%), bisdemethoxycurcumin (3%), and cyclocurcumin (3%). For centuries, people have turned to this natural remedy to alleviate swelling and speed the recovery of damaged skin wounds. The topical administration of curcumin has been shown to aid in the body's natural wound healing process. The wound-healing process is aided by curcumin because it works at several stages, including the inflammatory, maturation, and proliferative stages.[16,17] It is FDA-approved and has several biological actions, including anti-inflammatory and antioxidant effects.[18] The unique chemical structure of curcumin (CUR) allows it to engage with several molecules, resulting in its capacity to donate or accept H-bonds and bind with multivalent cations.[19] CUR's antioxidant properties are well known due to its effect on reactive oxygen species (ROS) such as superoxide anion, hydrogen peroxide, peroxyl radicals, hydroxyl radicals, and singlet oxygen.[20] The anti-inflammatory actions of CUR are linked to its capacity to alter cell signalling molecules. Studies have found that CUR affects signal transducers and transcription activators such as Notch-1, Nrf2, JAK-STAT, NF-kB, and protein kinases Akt and MAPK.[21,22] The anti-inflammatory properties of CUR target and reduce skin inflammation in several skin disorders by lowering immune cell cytokine expression.[23] However, the clinical efficiency of curcumin is limited by variables including low bioavailability, water solubility, and quick metabolism. Another drawback of curcumin is topical toxicity at high dosages.[15–17]

To overcome these constraints, CUR has been incorporated using advanced delivery systems including micro-sponges,[24] hydrogels,[25] nanoparticles,[26] nanofibers,[27] emulsions,[28] and lipid-based nanoparticles.[29] Recent developments in nanostructured lipid carrier (NLC) formulations, composed of a specific combination of solid and liquid lipids, have garnered significant interest due to their chemical stability, low toxicity, and impressive loading and entrapment efficiency. Unlike solid lipid nanoparticles (SLN), NLCs represent an advanced form of lipid nanoparticles (LNPs), demonstrating low toxicity due to their biocompatibility and biodegradability. Their disorganised crystal structure, characterised by reduced crystallinity, limits drug leakage and enhances drug payload capacity.[30] Therefore, employing nano delivery technologies to regulate the limiting factors of curcumin presents an interesting approach to leverage its wound healing capabilities. Nonetheless, these also present specific constraints, including a low surface-to-volume ratio, inconsistent release kinetics, inadequate mechanical conditions for cellular invasion and proliferation, and issues related to stability.

The present study seeks to develop a 3D bioprinted composite of poly(lactic acid) and curcumin incorporated into NLCs. This approach aims to mitigate some of the limitations linked to traditional NLCs when utilised independently, presenting a promising strategy for enhancing wound healing and furthering applications in regenerative medicine. This 3D bioprinting method facilitates accurate and personalised administration of therapeutic agents directly to the wound area, allowing for regulated release within specifically designed structures that correspond to the wound's shape and size, thereby enhancing healing effects and possibly aiding in tissue engineering.[31,32] Poly(lactic acid) (PLA) is a biodegradable polymer commonly employed in 3D bioprinting, especially in applications related to tissue engineering and regenerative medicine. The widespread appeal of PLA arises from its compatibility with biological systems, its ability to break down naturally, and its robust mechanical properties.[33] Unlike other biopolymers, such as polycaprolactone (PCL) or polylactic-*co*-glycolic acid (PLGA), PLA degrades into non-toxic byproducts, primarily lactic acid, which are metabolized naturally through the body's Krebs cycle, minimizing the risk of inflammatory responses or cytotoxic effects.[34,35] PLA also offers a more balanced degradation rate compared to PCL, which degrades in a significantly slower manner and may impede timely tissue regeneration in dynamic wound environments. Mechanically, PLA exhibits superior tensile strength and thermal stability, which are critical for maintaining scaffold integrity during the healing process, unlike PLGA, which often displays lower mechanical robustness and faster degradation that may compromise structural support.[36,37] In the realm of skin regeneration, PLA scaffolds act as a temporary platform for cellular proliferation, closely resembling the natural skin structure, providing mechanical support, and directing cell growth.[38] As PLA scaffolds degrade over time within the body *via* natural metabolic processes, they convert into non-toxic substances, eventually being replaced by the newly formed tissue.[39]

The novelty of the present study lies in the development and integration of curcumin-loaded nanostructured lipid carriers (CNLC) into 3D bioprinted PLA scaffolds for wound healing, marking a pioneering approach in combining the therapeutic benefits of curcumin with advanced 3D bioprinting technology. This is the first reported study to leverage CNLC's capacity to enhance curcumin's bioavailability and stability—overcoming its inherent limitations such as poor solubility and rapid metabolism—within a structurally and biologically favourable PLA scaffold matrix. The integration of CNLC into a 3D bioprinted scaffold not only ensures controlled and localized drug delivery but also addresses challenges in traditional drug delivery systems by offering precise customization to wound sites. Following this, we delved into an analysis of the physicochemical attributes exhibited by the 3D-bioprinted PLA/CNLC scaffold. Also, this biomaterial was

employed to scrutinize the *in vitro* proliferation of the 3T3 human fibroblast cell line. Moreover, we also conducted *in vivo* experiments using rats bearing full-thickness wounds to evaluate the efficacy of these fabricated scaffolds in fostering wound healing. By merging nanotechnology with 3D printing, this approach sets a new benchmark in regenerative medicine, particularly for wound healing applications, and opens avenues for personalized therapeutic interventions.

2. Experimental

2.1 Materials and methods

2.1.1 Materials. Highly pure (>95%) curcumin and Tween 80 obtained from Sigma Aldrich, India were used as the API and surfactant, respectively. Stearic acid and oleic acid required to synthesize CNLC were acquired from HiMedia Chemicals, Mumbai, India. Nature Tec India Pvt. Ltd provided PLA (grade: 3D850 M_w = 116 000 g mol^{-1}) which was utilised as a biopolymer in the fabrication of scaffolds.

2.2 Preparation of CNLC

Blank NLCs (BNLC) and curcumin loaded NLCs (CNLC) were developed in accordance with the melt dispersion ultrasonication technique with slight modification.[40] The overall procedure is stated below which includes two stages. An oil phase made up of a 3 : 1 mixture of the lipids stearic acid (solid) and oleic acid (liquid) was prepared. An aqueous phase containing 2% Tween 80 in distilled water was prepared. Separately, 1% curcumin was added in the above mixture for the preparation of CNLC. Both phases were first heated independently to 80 °C until the lipid melted and formed a homogeneous clear lipid phase. Following the melting process, the lipid phase was mixed with the surfactant aqueous solution at 2000 rpm for 10 min while maintaining the same temperature. The obtained pre-emulsion was subjected to further treatment with a probe-type ultrasonicator (make: Sonics & Materials, Inc.; model: Sonics VibraCell), with an on time of 6 s and an off time of 3 s, for 15 min, at a temperature that was kept at least 5 °C above the melting point of the lipids. Then, the dispersions were allowed to cool to room temperature. The procedure for the preparation of blank NLCs was the same except for the addition of curcumin to the NLCs.

2.2.1 Preparation of bioinks. After adequate pre-drying, 10 g of PLA pellets were weighed into a beaker containing 30 mL of chloroform. For at least 3 h, the mixture was agitated to ensure that all of the PLA was homogenously dissolved. To prepare the curcumin loaded PLA (PLA/C) scaffold, 100 mg of curcumin was added to the PLA/chloroform solution. In order to prepare the PLA/CNLC sample, 10 mL of CNLC was added to the PLA/chloroform solution separately. Both of these combinations were agitated for an additional 12 h to ensure that the NLC content was evenly distributed throughout the PLA matrix.

2.2.2 Fabrication of 3D bioprinted scaffolds. In this work, an advanced 3D bioprinter based on pneumatic extrusion (Cellink BioX^{TM}, Sweden) was used to construct 3D bioprinted PLA, PLA/C, and PLA/CNLC scaffolds. Auto CAD SolidWorks was used to create the 3D porous structure in the scaffolds. The dimensions of each 3D sample were standardised to be 10 × 10 × 1 mm. Each scaffold was printed by depositing a layer of biomaterial *via* a nozzle with a diameter of 0.41 mm. The printing speed and pneumatic pressure were both fixed at 2 mm s^{-1} and 120 kPa, respectively. An orthogonal layer arrangement of 0/90° was used for the fabrication of 3D bioprinted scaffolds.

2.3 Characterization of NLCs and bioinks

2.3.1 Particle size analysis. Dynamic light scattering (DLS) (make: Anton Paar Litesizer; model: 500) was used to determine the particle size of CNLC. Polydispersity index (PDI) and hydrodynamic diameter (mean diameter, *z*-average) are two parameters of particle size distribution that may be obtained using DLS. All samples were diluted (10×) with ultra-pure water before measurements and were used to achieve an appropriate scattering intensity. The optimal temperature during the measurement was 25 °C.

2.3.2 Zeta potential analysis. The electrophoretic mobility was measured to obtain the zeta potential (ZP) of the CNLC dispersion (make: Anton Paar Litesizer; model: 500). Three separate measurements were taken for each sample at 25 °C.

2.3.3 Entrapment efficiency and drug loading. Successful drug entrapment into the nanocarrier system is quantified as the entrapment efficiency (EE) of the drug. This is determined relative to the total quantity of the active drug included in the formulation (eqn (1)). However, the quantity of drug integrated into the nanocarrier system is quantified by its drug loading capacity (DL). It is determined relative to the total mass of the formulation (eqn (2)). The centrifugation method was used to determine the percentage of drug loading and the entrapment efficiency of CNLC. The pH of CNLC was lowered to 1.2 with the addition of 0.1 N HCl to form aggregates. After this, the NLC was centrifuged at 12 000 rpm for 60 min. Following the collection of 1 mL of supernatant, 9 mL of methanol was further added to make up the volume to 10 mL. The concentration of curcumin in the above solution was determined in triplicate using a UV-spectrophotometer at a wavelength of 423 nm.[33] Eqn (1) and (2) were used to calculate the %EE and %DL parameters for CNLC.

$$\%\mathrm{EE} = \frac{\text{Total amount of curcumin} - \text{amount of free curcumin}}{\text{Total amount of curcumin}} \times 100 \quad (1)$$

$$\%\mathrm{DL} = \frac{\text{Total amount of curcumin} - \text{amount of free curcumin}}{\text{Total amount of NLC}} \times 100 \quad (2)$$

2.3.4 Morphological analysis. Field emission scanning electron microscopy (FE-SEM) (make: Carl Zeiss, Germany;

model: Supra 35 VP) was used to examine the exterior surface morphology of CNLC and determine their shape. Distilled water was used to dilute the samples, which were further air-dried, sputtered with gold under vacuum, and then subjected to FESEM examination at 4.0 kV.

2.4 Rheological characterization

The rheological characteristics of 3D printable bioinks of PLA, PLA/C, and PLA/CNLC were evaluated using a rotating rheometer (make: Thermo Scientific, Karlsruhe, Germany; model: HAAKETM MARSTM iQ). All rheology studies were conducted on a 60 mm parallel plate. The measurements were conducted at 25 °C. Before the analysis, the equipment was calibrated to a shearing rate of 1–100 s^{-1} for 300 s to ensure accuracy. Rotational measurements were conducted at shear rates ranging from 0.01 to 100 s^{-1}.

2.5 Characterization of 3D bioprinted scaffolds

2.5.1 Fourier transform infrared (FTIR) spectroscopy analysis. FTIR spectroscopy (make: Bruker Optik GmbH, Germany; model: TENSOR 27) was used to conduct the spectral studies of curcumin, BNLC, and CNLC. The existence of functional groups in 3D bioprinted PLA, PLA/C, and PLA/CNLC scaffolds was also examined, and spectra were obtained in the wave number range of 4000–400 cm^{-1}. The curcumin, BNLC, and CNLC samples were pelletized using a die pressing process after being combined with dried KBr at a mass ratio of 1 : 10 to facilitate analysis. The spectra for 3D bioprinted composite scaffolds were obtained using the attenuated total reflectance (ATR) mode.

2.5.2 X-ray diffraction (XRD) analysis. The structural analysis of curcumin, BNLC, CNLC, and 3D bioprinted PLA, PLA/C, and PLA/CNLC scaffolds was conducted using an XRD analyser with Cu Kα radiation (1.54 Å) (manufacturer: Rigaku; country: Japan; model: Smart Lab Guidance). Wide-angle X-ray spectra (WAXS) were captured at a scan rate of 3° min^{-1} with a 2θ detection range of 10° to 60°. The experiment was performed using a step size of 0.01° and a counting time of 0.5 s per step at 40 kV and 30 mA.

2.5.3 Thermogravimetric analysis (TGA). Using a thermogravimetric (TG) analyser (make: NETZCH, Germany; model: STA 2500), the heat stability or thermal degradation behaviour of curcumin, CNLC, BNLC, and 3D bioprinted PLA, PLA/C, and PLA/CNLC composite scaffolds was assessed. All samples were analysed in the temperature range of 30–600 °C at a heating rate of 10 °C per minute in a nitrogen (N_2) environment.

2.5.4 Scanning electron microscopy (SEM) analysis. 3D bioprinted PLA, PLA/C, and PLA/CNLC composite scaffolds were examined for their surface morphology using a scanning electron microscope (make: TESCAN, Czech Republic; model: VEGA 3). Before being analysed by SEM, the scaffolds were gold-sputtered under vacuum.

2.5.5 Atomic force microscopy (AFM) analysis. Atomic force microscopy in the contact mode (make: Agilent Technologies, USA; model: 5500 series) was utilized to examine the surface topography of 3D bioprinted PLA, PLA/C, and PLA/CNLC composite scaffolds.

2.5.6 *In vitro* degradation analysis. For the *in vitro* degradation investigation, 3D bioprinted scaffolds of PLA, PLA/C, and PLA/CNLC (1 cm × 1 cm) were dry-weighed (W_o) before being immersed in a 5 mL vial of phosphate buffer solution (PBS) (pH 7). The vials were kept in an orbiting incubator rotating at 100 rpm and 37 °C for up to four weeks. The samples were taken out of the vials after 1, 7, 14, 21, and 28 days and then freeze dried and weighed (W_d). By comparing the post-degradation weight of the sample to its initial weight, the percentage of scaffold degradation was calculated using the formula given below:

$$\text{Weight loss}\,(\%) = \frac{W_o - W_d}{W_o} \times 100 \quad (3)$$

2.5.7 Antibacterial activity. The evaluation of antibacterial activity of the scaffolds was conducted through the agar disc diffusion method, using Gram-positive (*Staphylococcus aureus*) and Gram-negative (*Escherichia coli*) bacterial strains. In a solution of 0.9% NaCl in 3 mL of deionized water, the microorganisms were suspended. The agar medium was prepared by combining the microbial suspension with it shortly before it could solidify. The bacterial suspension contained about 3×10^7 CFU of bacteria per millilitre. First, 15 mL of the agar medium containing the bacteria was evenly distributed across Petri dishes and allowed to solidify. Then, the 3D bioprinted PLA, PLA/C, and PLA/CNLC scaffolds (1 cm × 1 cm) were gently positioned on the agar. After this, the Petri dishes were kept at 37 °C for 24 h. Using the antibiotic zone reader, the size of the zone of inhibition was measured to determine the efficacy of the scaffolds.

2.6 *In vitro* cell culture studies

The 3 T3 mouse embryonic fibroblast cell line was obtained from the National Centre for Cell Science (NCCS), Pune, India, for *in vitro* biological assessment experiments. Given the importance of fibroblasts in the connective tissue, this cell line has been used extensively in research to investigate wound healing in *in vitro* models, which makes it an ideal preference for this study. The 3 T3 cell line was cultured in Dulbecco's Modified Eagle's Medium (DMEM, Gibco™, USA). Also, the medium was supplemented with foetal bovine serum (FBS) and antibiotics [penicillin (100 g mL^{-1}) and streptomycin (100 g mL^{-1})]. The culture was incubated at 37 °C in an environment containing 5% CO_2. All cell culture experiments were done in triplicate.

2.6.1 Cell proliferation assay. For this study, 3 T3 cells were seeded onto 3D bioprinted PLA, PLA/C, and PLA/CNLC composite scaffolds and then subjected to an MTT [(3-(4,5-dimethylthiazolyl-2)-2,5-diphenyltetrazolium bromide), Sigma Aldrich, India] assay to determine the vitality and proliferation of the cells. The MTT reagent was prepared by diluting it to a concentration of 5 mg mL^{-1} in phosphate buffer solution (PBS, Gibco™, USA) prior to use. Cell-seeded scaffolds were incubated for the appropriate time (1–14 days), 40 μL of MTT solution was

added, and then the scaffolds were left in the incubator for another 4 h, until a purple precipitate was formed. The yellow MTT dye was reduced by the mitochondrial oxidoreductase enzyme in cells with active metabolism. Then, the media was sucked out of all the wells, and were washed thrice with PBS. After the medium was removed, 300 μL of dimethyl sulfoxide (DMSO, Sigma-Aldrich, India) was added to dissolve the formazan crystals for spectroscopic analysis. The microplate reader was then used to evaluate the cytotoxicity of 3 T3 cells by measuring the OD at 570 nm (make: Thermo Fisher Scientific, Waltham, USA; model: Multiskan GO). The following formula was used to determine the percentage (%) of live cells:

$$\text{Cell viability}\,(\%) = \frac{(\text{mean value of OD})_{\text{test}}}{(\text{mean value of OD})_{\text{control}}} \times 100 \quad (4)$$

2.6.2 Live/dead assay. The 3D bioprinted PLA, PLA/C, and PLA/CNLC composite scaffolds were stained with Acridine Orange/Ethidium Bromide (AO and EtBr, HiMedia, India) to analyse the apoptotic behaviour of cells. After the 7th and 14th day of the incubation period, the cell-seeded 3D bioprinted scaffolds underwent three washes with sterile PBS and were subsequently stained using a dual fluorescent solution containing AO and EtBr. The cells underwent incubation for 45 min prior to visualisation with a fluorescent cell imager (model: ZOETM; manufacturer: Bio-Rad Laboratories, Singapore). The observation of green fluorescence signifies the presence of viable cells, as AO is capable of penetrating living cells and attaching to DNA within the nucleus. EtBr infiltrates compromised cell membranes and interacts with fragmented DNA, resulting in red fluorescence, indicative of cell death.

2.7 *In vivo* animal wound model

An excision wound model in adult male Wistar rats was used to test the wound healing efficiency of 3D bioprinted composite scaffolds. All rats used in the investigation were pathogen-free and weighed between 150 and 200 g (Kedar Biolabs, Telangana, India). The animals used in the research were obtained from the primary animal facility available at SPMVV University, Tirupati, India. The Institutional Animal Care and Use Committee (IACUC) granted approval for this study, with approval number CPCSEA/1677/SPMVV/IAEC/III. The rats were housed in polypropylene cages at a temperature of 25 ± 2 °C and subjected to a standard 12 h laboratory light/dark cycle. Food (chow) and water were always available to the rats. There were 24 animals overall, and they were divided into four sets of six each (Table 1). The first group (control) received no treatment. The second group received a blank (PLA) scaffold, the third group received a curcumin loaded PLA scaffold (PLA/C), and the fourth group received a PLA scaffold incorporated with CNLC (PLA/CNLC). Each group received a scaffold with an area of 1 cm^2.

2.7.1 Preparation of animals. Prior to being placed in a natural resting position on the operating table, the animals were given intramuscular injections of xylazine HCl (10 mg kg^{-1}) and ketamine HCl (80 mg kg^{-1}) to induce anaesthesia. The dorsal fur of the animals was shaved using an electric clipper, and an outline of the planned wound location, measuring 1 × 1 cm^2, was sketched on their backs, between their shoulders (5 mm away from the ears). A 1 cm^2 wound area was obtained after the full-thickness skin had been removed from the designated region. This wound was then cleaned with sterile gauze to restore equilibrium. After receiving their respective scaffolds, the animals in the treatment groups (groups II, III, and IV) were bandaged. Every day, the bandage wrap was checked for looseness and changed, if necessary, until the 28th day.

2.7.2 Wound closure. The percentage of wound healing was recorded every week after the infliction of the wound. The graphical method was employed to ascertain the percentage reduction in the wound area by tallying the squares of the retraced wound area. The proportion of the original wound area healed was calculated using the following eqn (5):

$$\%\text{closure} = 1 - \frac{\text{wound area on zeroth day}}{\text{wound area on the following days}} \times 100 \quad (5)$$

Table 1 Treatment groups for *in vivo* studies

S. no	Group no	Group name	No. of animals	Treatment
1.	I	Wound	6	Wound created
2.	II	Blank	6	Wound created + PLA scaffolds
3.	III	Test I	6	Wound created + PLA/C scaffolds
4.	IV	Test II	6	Wound created + PLA/CNLC

2.8 Assessment of biochemical constituents

The granulation tissue of all the animals was collected on days 7 and 14. After being washed in cold saline (0.9%) to eliminate any blood clots, the sample was stored in a normal saline solution at −20 °C until biochemical analysis could be conducted.

2.8.1 Estimation of hydroxyproline. Following the procedure outlined by Ponrasu *et al.*,[41] the hydroxyproline concentration of the connective tissue surrounding the wound was determined. Briefly, 10 mL of 6 N HCl was used to homogenise 300 mg of granulation tissues, and the resulting liquid was afterwards transferred into test tubes. The test tubes were sealed, and then heated to 130 °C for 3 h to hydrolyze the samples. The contents of the test tubes were transferred to a graduated measuring cylinder, 2 mL of methyl red was added, and the cylinder was shaken briskly. Then, NaOH (2.5 N) was added, and the solution was agitated until the pink colour faded to yellow. The pH was adjusted to a more neutral range by adding HCl (0.01 N), to around 6–7. By diluting with distilled water, the total volume of the sample was brought to 50 mL, and then 2 mL of the diluted sample was mixed with 1 mL of chloramine-T solution. To this, 1 mL of perchloric acid was added and the contents were kept at room temperature for 20 min after gentle mixing. Each test tube was added with 1 mL of *p*-dimethylaminobenzaldehyde (PDAB), and then they were shaken until there was no longer any trace of colour.

Each tube was heated to 60 °C in a water bath and subsequently cooled rapidly under running water. The absorbance was recorded at 557 nm with the use of a calorimeter. The tissue hydroxyproline concentration was determined using a standard curve and expressed as mg g^{-1} wet weight.

2.8.2 Estimation of hexosamine. The Blix method was employed to ascertain hexosamine concentrations across various body tissues. To achieve this, 300 mg of granulation tissues was homogenised in 10 mL of 6 N HCl, and subsequently, the solution was transferred into test tubes. The samples were hydrolyzed by placing them in sealed test tubes and heating them to 98 °C for 8 h. The pH was adjusted to 7 by adding 4 N NaOH to the solution in the test tubes, which were then poured into the graduated cylinder. The sample was diluted to 50 mL with distilled water, and then 2 mL of that solution was mixed with 1 mL of 2% acetylacetone. After heating the mixture to 96 °C for 40 min, 1 mL of Ehrlich's reagent and 5 mL of 96% ethanol were added, and the liquid was cooled under running water. The solution was then stirred and allowed to stand still for 1 hour at room temperature. The absorbance of the pink solution was recorded at 530 nm, and the concentration of hexosamine was established by referencing the results against a standard curve. The hexosamine content of the tissue is presented in mg g^{-1} of dry weight.

2.9 Histological analysis

On days 7, 14, 21 and 28 of therapy, histological samples were obtained from all groups and preserved in 10% buffered formalin. Sections were cut using a corneal trephiner and stained with hematoxylin and eosin following the normal protocol of paraffin embedding. The fixed samples were examined under a microscope to determine the effect of 3D bioprinted scaffolds on wound healing.

2.10 Gross studies

The photographs of wounds sustained by each group were captured and compared visually as part of our overall assessment.

2.11 Statistical analysis

The results are presented as the mean standard deviation (S. D.), and all studies were performed in triplicate. The statistics were analysed using GraphPad Prism® 7 (Version 7.0). One-way ANOVA was carried out for three or more groups to determine the statistical significance. Statistical significance (when $n = 3$) was assumed for values with p-values of $^{*}p < 0.05$, $^{**}p < 0.01$, $^{***}p < 0.001$, and $^{****}p < 0.0001$.

3. Results and discussion

3.1 Size distribution, zeta potential and morphology

To enhance the bioavailability of curcumin, NLCs containing curcumin were produced using the melt dispersion ultrasonication process. Stearic acid was used as the solid matrix and oleic acid was used as the liquid lipid for the production of CNLC. Tween 80 was chosen as a surfactant. In the context of NLCs, particle size is a crucial factor that influences both the degree and speed at which a drug may permeate and be deposited in the skin. The particle size study of CNLC indicates that they exhibit a slim distribution width and a narrow particle size range of 200–500 nm with polydispersity indexes (PDI) of 0.173, which confirms the homogeneity of the dispersion (Fig. 1(a)). A smaller particle size results in a greater interfacial surface area, which enhances medication absorption. Particles with an average diameter of up to 400 nm may be readily carried across cells. Furthermore, it was proposed that the reduced dimensions facilitate a more rapid rate of release.[42] Additionally, there have been reports indicating that a smaller particle size might result in faster absorption and enhance the bioavailability.[43] Additionally, PDI quantifies the breadth of particle size dispersion. If the polydispersity index (PDI) is less than 0.5, it indicates a high level of uniformity in the particle population. Conversely, high PDI values indicate a wide range of particle sizes.

The ZP denotes the electric charge applied to the surface of the NLCs. A higher ZP value indicates a better likelihood of stability for the suspension, since the charged particles resist each other and counteract the inherent inclination to assemble. It is widely accepted that larger ZP values, whether positive or negative, indicate that the dispersion will exhibit more long-term stability.[44] The ZP value was determined to be −10.41 mV (Fig. 1(b)). Formulations with a negative zeta potential experience stronger electrostatic repulsion between globules, which prevents the merging of globules and ensures their physical stability.

The morphological analysis of the NLC formulation was conducted by capturing Field Emission Scanning Electron Microscopy (FESEM) images of freeze-dried NLCs. It has been revealed that they possess an oval form (Fig. 1(c)). The size analysis findings align with the size distribution histogram obtained from the FESEM study for CNLC (Fig. 1(d)).

3.2 Encapsulation efficiency and drug loading

The developed CNLC showed satisfactory entrapment and loading efficiency. The entrapment efficiency of curcumin was determined to be 81.37 ± 0.85%, whereas the drug loading was found to be 6.59 ± 1.61%.

3.3 Rheological characteristics of bioinks

The rheological characteristics of bioinks is a crucial foundation for assessing their capacity to be printed. A suitable viscosity is needed for the bioink in order to achieve high form fidelity and controlled printing. The objective is to develop an ink that has a well-defined yield stress and exhibits shear-thinning behaviour in terms of rheology. The bioink must possess sufficient strength to prevent the building from collapsing due to its own weight after deposition.[45]

Fig. 2(a) demonstrates that the storage modulus (G') has a positive correlation with frequency for all three inks, suggesting their elastic nature. The material PLA/CNLC exhibits the greatest value of G', followed by PLA/C, and finally PLA. This indicates that PLA/CNLC has the highest elasticity

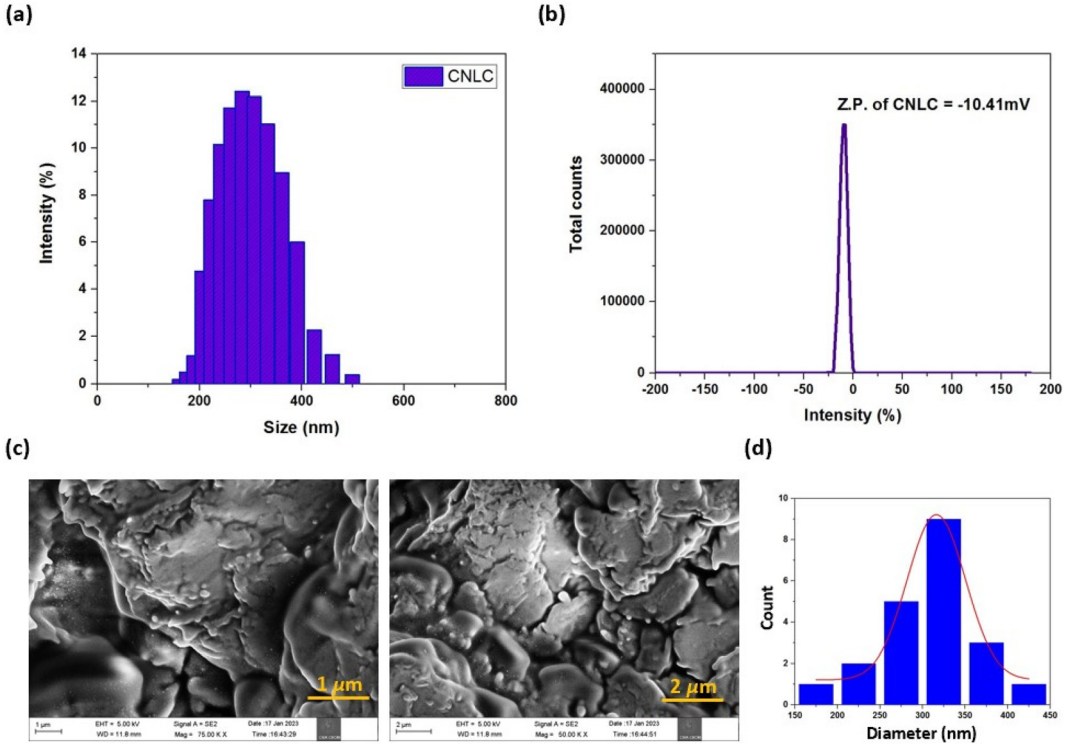

Fig. 1 (a) Particle size distribution, (b) zeta potential, (c) FESEM images, and (d) particle size distribution histogram for CNLC.

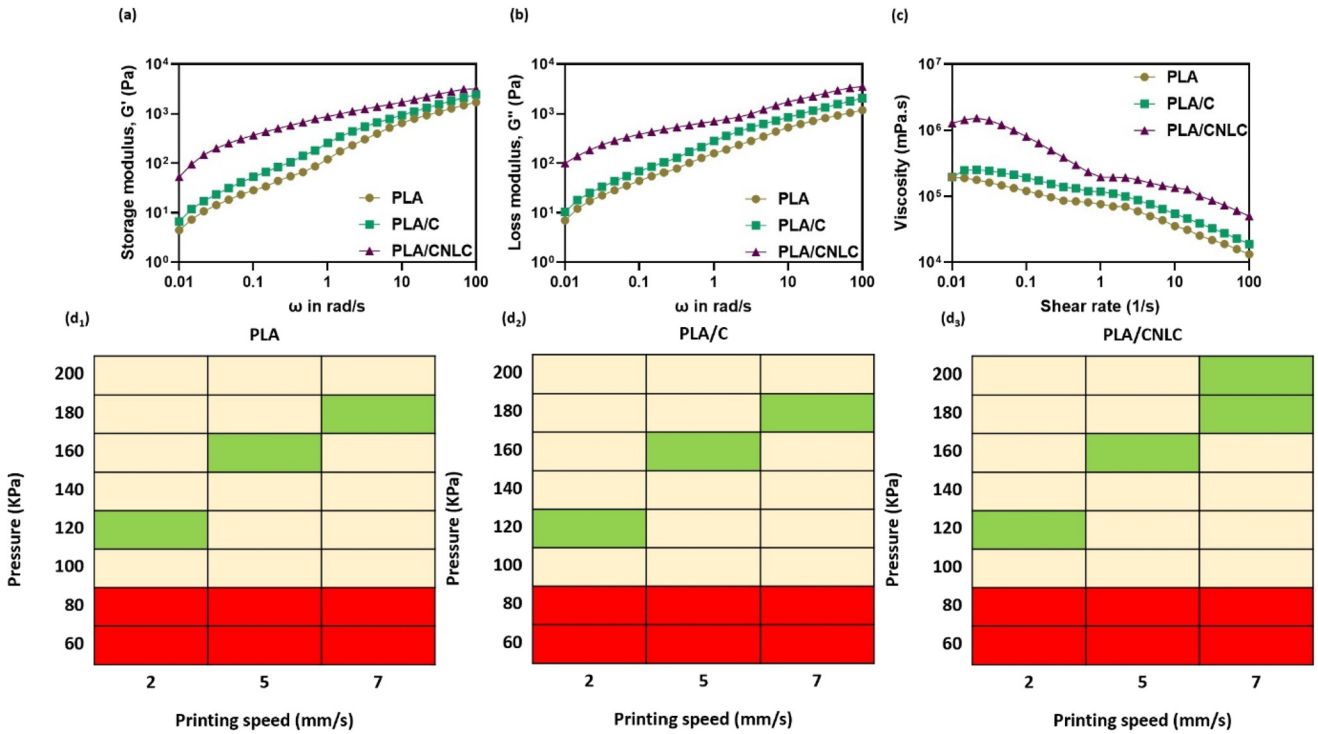

Fig. 2 (a–c) Rheological properties of 3D printable PLA, PLA/C and PLA/CNLC bioinks. (d_1–d_3) Optimization of parameters for 3D printable PLA, PLA/C and PLA/CNLC bioinks.

and has the capacity to store a greater amount of energy throughout the process of deformation. Fig. 2(b) illustrates the loss modulus (G''), which likewise exhibits an increase in the value as the frequency rises. The PLA/CNLC combination once again demonstrates the greatest values, with PLA/C and PLA following closely after. Furthermore, they exhibit a $G' < G''$ relationship. At a shear rate of 0.01%, the storage modulus (G') of PLA is 6 Pa and the loss modulus (G'') is 8 Pa. At the same shear rate, PLA/C has G' and G'' values of 8 and 12 Pa, while PLA/CNLC has higher G' and G'' values of 72 and 108 Pa, respectively. Consequently, it may be inferred that the viscosity of the bioink is more significant than its elasticity, which is a typical characteristic of any polymeric bioink.

The viscosity of the bioink was measured at a temperature of 25 °C throughout a range of shear rates from 0.01 to 100 Hz (Fig. 2(c)). The rheological investigation revealed that the viscosity of PLA at a frequency of 0.01 Hz was found to be 19×10^4 Pa s. However, at the greatest shear rate of 100 Hz, the viscosity reduced significantly to 13×10^3 Pa s. The viscosity of PLA/C was found to be 19×10^4 at a frequency of 0.01 Hz and reduced to 18×10^3 Pa s at the greatest shear rate of 100 Hz. The viscosity of the PLA/CNLC mixture was initially found to be 12×10^5 at 0.01 Pa s and decreased to 15×10^3 when subjected to the greatest shear rate of 100 Hz. All three bioinks showed shear-thinning characteristics and PLA/CNLC exhibited the highest viscosity compared to other bioinks, where the viscosity decreased as the shear strain increased. Hence, all three bioinks demonstrated unobstructed extrusion *via* the 3D printer nozzle, indicating their compatibility with 3D-bioprinting.

The extrusion tension and printing speed were adjusted to control the optimal circumstances for 3D printing with PLA, PLA/C, and PLA/CNLC. Various printing speeds ranging from 2 to 7 mm s^{-1} and extrusion pressures ranging from 60 to 200 kPa were used to print structures in order to assess the printability of all the bioinks in a qualitative manner (Fig. 2(d1–d3)). The printing outputs were categorised using the colours red, green, and yellow. The findings indicated that the colour red indicates the occurrence of blockage in the bio ink, while the colour yellow suggests the presence of a defective pore structure and geometry. On the other hand, the colour green signifies the optimal range for 3D printing. The bioink exhibited unobstructed flow from the nozzle and yielded very robust and functioning structures.

3.4 Fourier transform infrared (FTIR) spectroscopy analysis

FTIR analysis was used to determine the functional groups present in the active ingredient 'curcumin' and to investigate its interactions with lipid carriers. Fig. 3(a) displays the spectral pattern of curcumin, BNLC, CNLC, and the 3D bioprinted PLA, PLA/C, and PLA/CNLC scaffolds. The infrared spectra of curcumin include stretching vibrations at 1629 cm^{-1}, mostly associated with the overlapping stretching vibrations of alkenes (C=C) and carbonyl (C=O) functional groups. The infrared spectrum of the curcumin ligand exhibits a stretching vibration at 3180–3540 cm^{-1}, which is caused by the O–H groups. Furthermore, a C=C aromatic stretching vibration is observed at 1425 cm^{-1}, accompanied by a high intensity band at 1510 cm^{-1}. This band is associated with a combination of vibrations, such as the stretching of carbonyl bonds ν(C=O), in-plane bending vibrations related to aliphatic δ CC–C and δ CC=O, and in-plane bending vibrations concerning aromatic δ CC–H in both keto and enol forms. Additionally, stretching vibrations are observed around the aromatic C–C bonds in both the keto and enolic forms of curcumin.[26,46] Additionally, a notable and intense band at 1267 cm^{-1} corresponds to the bending vibration of the phenolic band ν(C–O). The spectra of BNLC and CNLC exhibit characteristic bands at 2919 cm^{-1} and 2851 cm^{-1}, which correspond to $-CH_2$ vibrations and O–CH_2 vibrations, respectively. Additional bands linked to ester bonds (–COO–) were seen at 1732 cm^{-1}, and vibrations relating to C=O and CH_2 were detected within the range of 1466–1202 cm^{-1}. Finally, the bands ranging from 966 to 1107 cm^{-1} are attributed to the symmetrical arrangement of the C–O bond and the asymmetric stretching vibrations of the C–O bond in the ether functional groups. Evidence of C encapsulation in lipid nanoparticles was indirectly discovered *via* the CNLC spectral analysis. The characteristic bands that typically indicate the presence of curcumin (C) were either hidden or concealed inside the blank Nano Lipid Carrier (NLC) peaks. The transmittance spectra of the pure PLA, PLA/C, and PLA/CNLC samples had distinct characteristics. Peaks were seen at 2700–3000 cm^{-1}, which correspond to the stretching of $-CH_2$ groups. Additionally, peaks at 1460–1413 cm^{-1} are ascribed to the bending of $-CH_3$ groups, while a peak at 1382 cm^{-1} is allocated to C–H bending. The picture also shows a clear elongation of the carbonyl group (C=O) in the ester bond at around 1749 cm^{-1}, along with a balanced elongation of the –C–O–C bond at 1170 cm^{-1} and an imbalanced elongation of the $-CH_3$ bond at 1070 cm^{-1}. The prominent bond seen in PLA/CNLC is characterised by peaks at 2923 cm^{-1} and 2856 cm^{-1}. Furthermore, the inclusion of CNLC in the PLA matrix reduced its peak intensities.

3.5 X-ray diffraction (XRD) analysis

X-ray diffraction (XRD) was used to investigate the crystalline characteristics of drug-loaded and drug-free nanostructured lipid carriers (NLCs). Highly crystalline lipids provide sharp, high-intensity reflections, whereas an amorphous backdrop of defective lipid lattice creates low-intensity reflections. Fig. 3(b) displays the X-ray diffraction patterns of curcumin, freeze-dried powder of blank BNLC, freeze-dried powder of CNLC, and the 3D bioprinted scaffolds made of poly(lactic acid) (PLA), PLA with curcumin (PLA/C), and PLA with curcumin-loaded NLCs (PLA/CNLC). The X-ray diffractogram of curcumin powder reveals distinct peaks at diffraction angles of 2θ = 12.99°, 14.86°, 17.23°, 17.91°, and 21.05°, indicating the presence of crystalline structure in the powder. The XRD pattern of CNLC shows the complete disappearance of the distinctive peaks associated with C, suggesting that C molecules have been dispersed inside the hydrophobic core region and have established a disordered connection with the NLC matrix. The

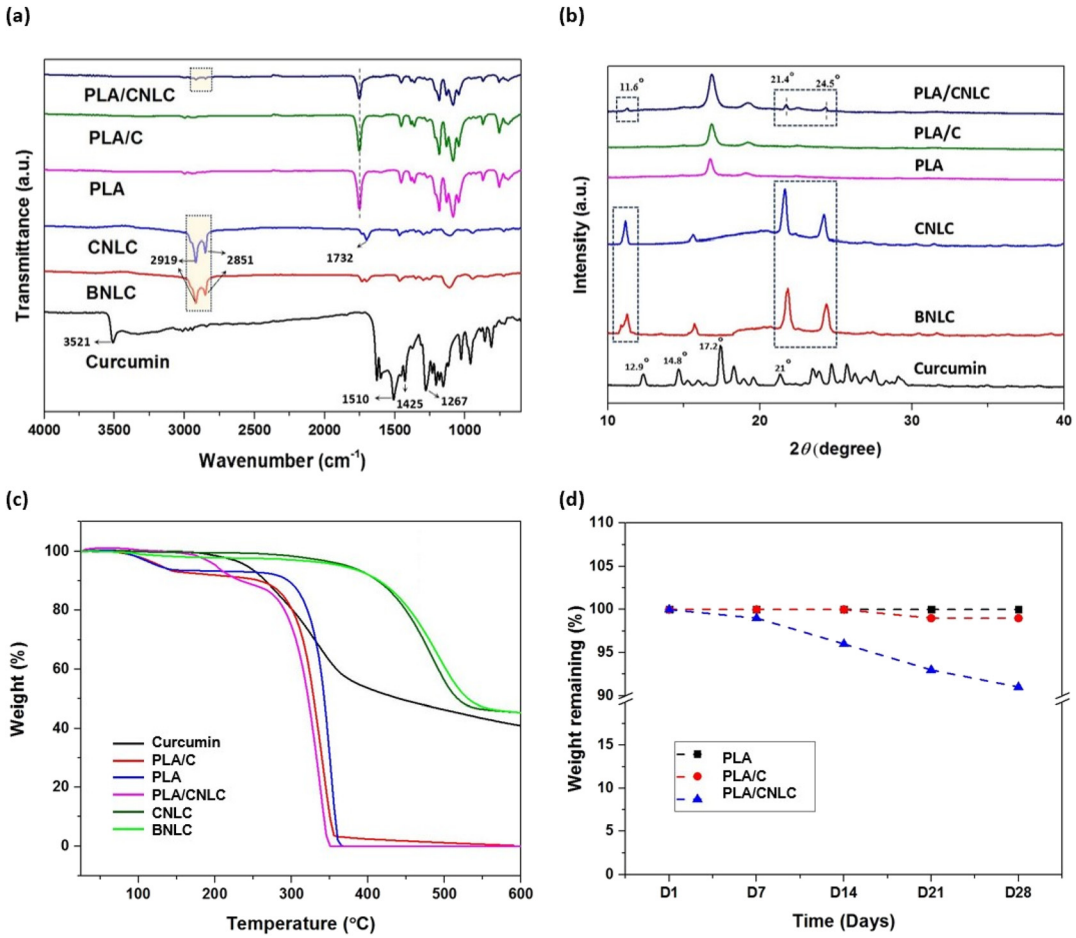

Fig. 3 (a) FTIR spectra, (b) XRD pattern, and (c) TGA profile for curcumin, BNLC, CNLC, and 3D bioprinted PLA, PLA/C, and PLA/CNLC scaffolds. (d) *In vitro* degradation study of 3D bioprinted PLA, PLA/C, and PLA/CNLC scaffolds in PBS solution (pH 7) at 37 °C.

diffraction pattern of both BNLC and CNLC shows no noticeable variation in the peak pattern, indicating that the addition of curcumin did not alter the characteristics of NLCs. The distinct diffraction peaks corresponding to PLA were identified in all of the 3DP scaffolds. The existence of CNLC may be confirmed from the presence of three low-intensity peaks in the diffractogram of PLA/CNLC, namely at 11.6°, 21.4° and 24.5°.

3.6 Thermogravimetric analysis (TGA)

Fig. 3(c) exhibits the thermogravimetric profile for curcumin, BNLC, CNLC, and 3D bioprinted PLA, PLA/C, and PLA/CNLC scaffolds. The graph shows that curcumin first underwent a decrease in mass between 85 and 120 °C, leading to a loss of around 3% of its mass. This behavior may be attributed to the process of water evaporation from the sample. The compound experienced a secondary reduction in mass as a result of thermal disintegration occurring between temperatures of 210 °C and 370 °C. The breakdown led to a reduction in mass of 58%. The residual mass constituted around 40% at a temperature of 599 °C. For both blank (BNLC) and drug-loaded NLCs, the sample experienced the greatest weight loss at higher temperatures, between 370 °C and 520 °C. The loss of integrity in lipid particles occurred as a result of the decomposition process, which includes the cleavage of the carbon–carbon double bond and the subsequent fragmentation of the molecule into smaller, volatile molecules.[47] The weight loss process in PLA/C occurs in two distinct stages. The first degradation stage takes place between temperatures of 85 and 148 °C, leading to a weight reduction of around 9%. The primary cause of this reduction in bulk is mostly attributed to the removal of moisture. The subsequent phase of degradation takes place within the temperature range of 260–355 °C, resulting in a significant decrease in mass by 96%. The thermogravimetric analysis (TGA) of the PLA/CNLC material reveals a substantial degradation process between temperatures of 180 °C and 347 °C, leading to a 98% reduction in mass. The main degradation mechanism in PLA/C and PLA/CNLC mainly consists of the breakdown of organic chains in C and CNLC, as well as the cleavage of the carbonyl backbone in PLA.

3.7 *In vitro* degradation study of 3D bioprinted scaffolds

Fig. 3(d) illustrates the findings of weight loss investigation carried out on scaffolds placed in PBS to obtain a deeper understanding of the degradation characteristics of 3D bio-

printed PLA and PLA composite scaffolds. The PLA and PLA/C scaffolds exhibited little weight loss; however, the degradation ratio markedly increased with the incorporation of CNLC into the scaffolds, as seen in Fig. 3(d). Based on these data, it can be inferred that the CNLC component plays a crucial role in regulating the degradation of the PLA/CNLC scaffold.

Table 2 Printing specifications used for the scaffold fabrication

Scaffolds	Nozzle diameter (mm)	Layer height (mm)	Avg. D_F (μm)	Avg. D_P (μm)
PLA	0.410	0.2	326	526
PLA/C	0.410	0.2	276	509
PLA/CNLC	0.410	0.2	626	201

3.8 Scanning electron microscopy analysis

Fig. 4 displays the results of the SEM study, which examines the morphology of the 3D bioprinted PLA, PLA/C, and PLA/CNLC composite scaffolds. Table 2 provides a comprehensive overview of the printing parameters associated with each scaffold. In this research, a 60% infill density was chosen for PLA and PLA/C, while a 50% infill density was picked for PLA/CNLC. This decision was made because of the observation that choosing a higher infill density led to the formation of non-uniform structures and blocking of pores. Choosing a lower infill density, however, led to uneven filament formation. The average pore diameter (Avg. D_P) and average filament diameter (Avg. D_F) of 3D bioprinted PLA, PLA/C, and PLA/CNLC scaffolds were determined from the SEM morphological analysis displayed in Fig. 4. The computed values are presented in Table 2. The PLA/CNLC composite scaffolds exhibit surface roughness, whereas the surfaces of PLA and PLA/C are smooth, as seen in Fig. 4. The level of roughness is directly related to the degree of uniform distribution of CNLC across the outside edges and inner regions of the PLA ink during the process of 3D printing. Fig. 4 shows the visual representations of the 3D bioprinted scaffolds.

3.9 Atomic force microscopy (AFM) analysis

Atomic force microscopy (AFM) was used to examine the surface and network topologies of the 3D bioprinted PLA, PLA/C, and PLA/CNLC scaffolds. AFM is a valuable technique for analysing the configuration and various characteristics of polymer nanocomposites. Fig. 5(a) illustrates that both PLA and PLA/C surfaces exhibit a rim-and-plain topology. However, the inclusion of CNLC into the PLA matrix resulted in a transformation of the topography into a rough surface with bristles. Therefore, the AFM surface topographical analysis uncovers the diverse and varied solid microstructure of PLA/CNLC scaffolds. Based on Fig. 5(b), the root mean square roughness (R_q) values are determined to be 53 nm for PLA, 92 nm for PLA/C, and 219 nm for PLA/CNLC. R_q is responsive to both the lower and higher frequency elements of the surface and offers quantification of the total roughness. PLA/CNLC exhibits more roughness as compared to other scaffolds.

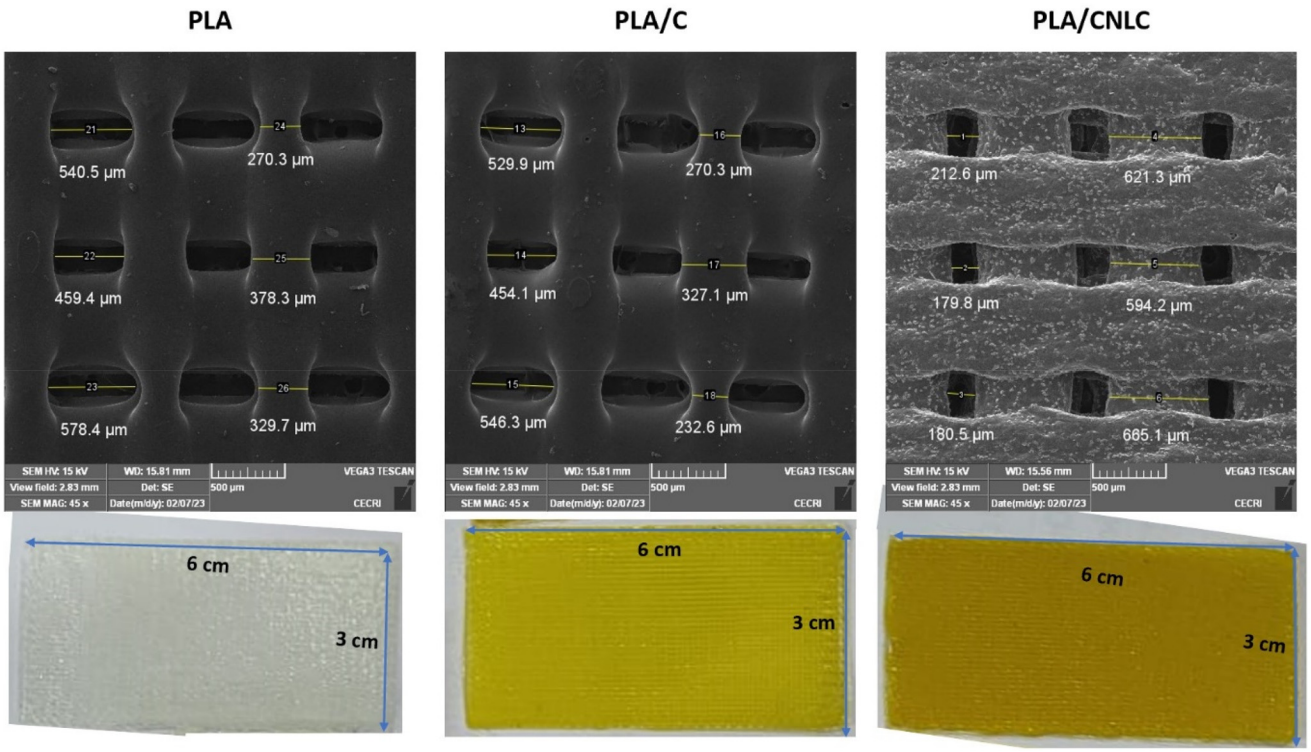

Fig. 4 SEM and optical images of 3D bioprinted PLA, PLA/C, and PLA/CNLC scaffolds.

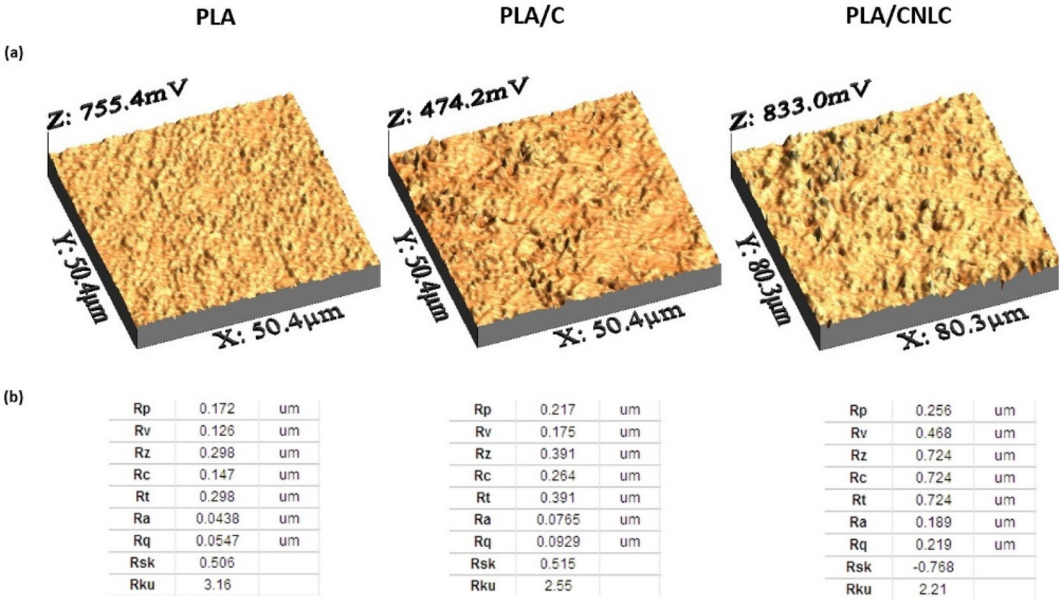

Rp	0.172	um
Rv	0.126	um
Rz	0.298	um
Rc	0.147	um
Rt	0.298	um
Ra	0.0438	um
Rq	0.0547	um
Rsk	0.506	
Rku	3.16	

Rp	0.217	um
Rv	0.175	um
Rz	0.391	um
Rc	0.264	um
Rt	0.391	um
Ra	0.0765	um
Rq	0.0929	um
Rsk	0.515	
Rku	2.55	

Rp	0.256	um
Rv	0.468	um
Rz	0.724	um
Rc	0.724	um
Rt	0.724	um
Ra	0.189	um
Rq	0.219	um
Rsk	-0.768	
Rku	2.21	

Fig. 5 (a) AFM surface topography and (b) roughness analysis for 3D bioprinted PLA, PLA/C, and PLA/CNLC scaffolds.

3.10 Antibacterial activity

The antibacterial efficacy of 3D bioprinted scaffolds is shown in Fig. 6(a) and (b). PLA/CNLC exhibited noteworthy antibacterial activities, yielding significant results. PLA/CNLC exhibited the highest zone of inhibition (ZOI) against *Escherichia coli* (2.6 cm) and *Staphylococcus aureus* (2.4 cm) when compared to PLA/C scaffolds. However, PLA/C demonstrated the ability to suppress the development of all bacterial strains, whereas PLA exhibited no antibacterial properties. The antibacterial activity observed in this study can be attributed to the unique properties of curcumin. Its mechanism of action involves the disruption of bacterial cell walls and membranes due to its interaction with lipid bilayers, which compromises membrane integrity.[48,49] This disruption is primarily facilitated by curcumin's hydrophobic polyphenolic structure, allowing it to embed into and destabilize bacterial membranes, leading to leakage of essential intracellular contents. Furthermore, curcumin induces oxidative stress by generating reactive oxygen species (ROS), which damage cellular components such as DNA, proteins, and lipids, ultimately resulting in bacterial cell death.[50] Additionally, curcumin is known to inhibit quorum sensing, a critical bacterial communication process, thereby reducing biofilm formation and virulence factor production.[51] These mechanisms collectively explain the observed enhanced antibacterial activity of the PLA/CNLC scaffolds against *Escherichia coli* and *Staphylococcus aureus*.

3.11 Cell proliferation assay

The biological compatibility of 3D bioprinted scaffolds made from PLA, PLA/C, and PLA/CNLC was assessed using the MTT

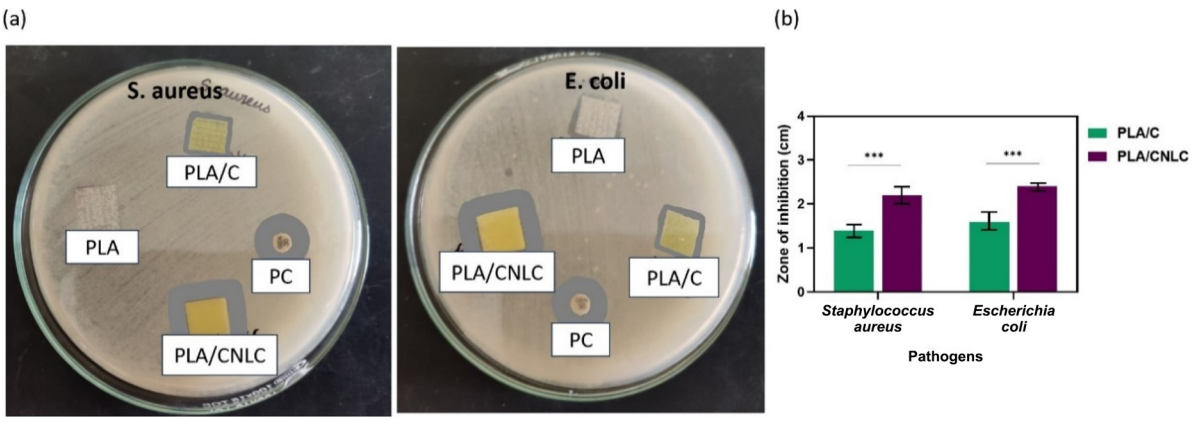

Fig. 6 (a) Antibacterial activity and (b) zone of inhibition graph for PLA/C and PLA/CNLC scaffolds for 3D bioprinted PLA, PLA/C, and PLA/CNLC scaffolds against Gram-positive and Gram-negative microorganisms.

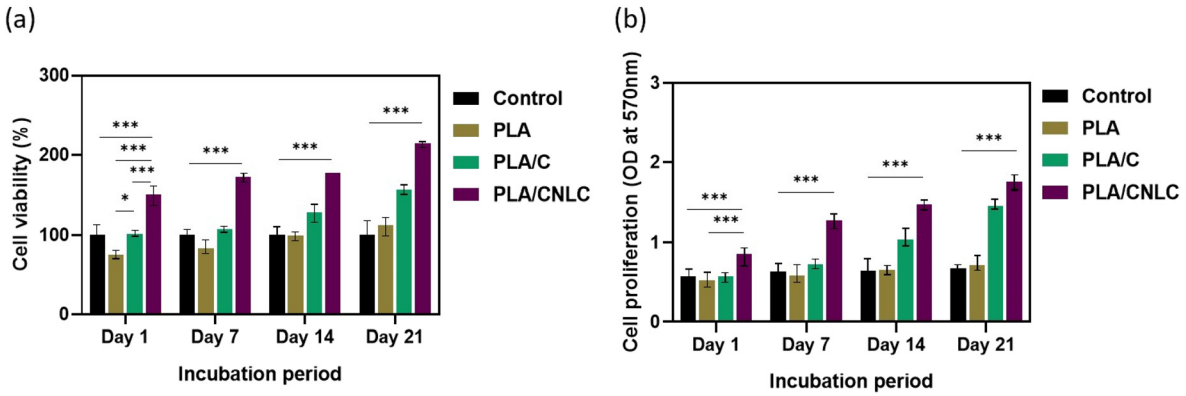

Fig. 7 Cell viability percentage and growth rate for 3D printed PLA, PLA/C, and PLA/CNLC scaffolds using MTT assay. (a) Viability percentage (%) *vs.* incubation period and (b) OD at 570 nm *vs.* incubation period. The data are presented as mean ± S.D. for $n = 3$. ** indicates significance for $p < 0.01$ and *** indicates $p < 0.001$.

test. The scaffolds were inoculated with 3 T3 cells, and the optical densities (ODs) were measured over a period of 1–14 days. Based on the data shown in Fig. 7(a), it can be inferred that the cell viability (%) of the PLA, PLA/C, and PLA/CNLC scaffolds increases as the incubation duration increases. The graph illustrates the percentage of cell viability throughout the period of 1 to 14 days of incubation. Fig. 7(b) demonstrates that the optical density of the PLA, PLA/C, and PLA/CNLC scaffolds increases as the incubation period progresses. The PLA/CNLC scaffolds exhibited the highest proportion of viable cells at all time periods, indicating that the scaffolds closely resembled the extracellular matrix (ECM) of the skin tissue and provided favourable conditions for cell growth, as seen by the cell proliferation shown in Fig. 7(b). The enhanced cell proliferation observed in the PLA/CNLC scaffolds can be attributed to the synergistic effects of curcumin's bioactive properties and the scaffold's optimized physical characteristics. Curcumin, as a potent antioxidant and anti-inflammatory agent, reduces oxidative stress in fibroblasts by neutralizing reactive oxygen species (ROS) and modulating inflammatory pathways.[52–55] This creates a favourable microenvironment that supports cellular viability, proliferation, and migration, which are essential processes in wound healing. Additionally, curcumin's ability to inhibit pro-inflammatory cytokines and promote the expression of growth factors further enhances fibroblast activity and tissue regeneration.[56,57] The PLA/CNLC scaffolds demonstrated superior performance compared to PLA and PLA/C scaffolds in terms of cell growth, providing evidence that their nanoscale design successfully replicated the extracellular matrix (ECM) and promoted cell attachment and proliferation.

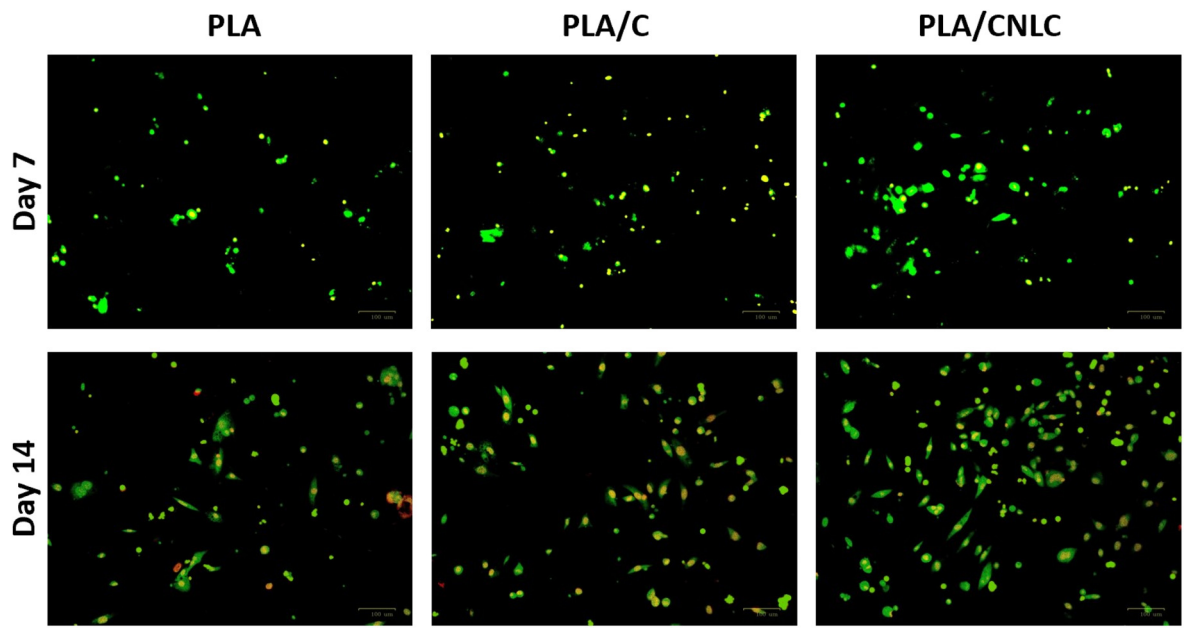

Fig. 8 Live/dead staining of 3 T3 cells seeded on PLA, PLA/C, and PLA/CNLC scaffolds for varying culture time durations.

3.12 Live/dead assay

The cell proliferation and vitality of 3 T3 cells on 3D bioprinted scaffolds made of PLA, PLA/C, and PLA/CNLC were evaluated and are shown in Fig. 8. Cells have the ability to colonise the scaffold when they are cultured for longer periods. Differentiating between normal cells and apoptotic cells may be achieved by assessing their permeability to AO and EtBr. Usually, the binding of DNA results in the emission of green glow for AO and red fluorescence for EtBr. Typically, deceased

Fig. 9 *In vivo* models of full thickness wound healing on the skin. (a) Photos of wound sites on days 0, 7, 14, and 21 after scaffold adhesion. (b) Statistical analysis of wound closure rates of the control, 3D bioprinted blank PLA, PLA/C, and PLA/CNLC groups at all time points.

cells exhibit vivid crimson luminescence and are readily susceptible to staining by both AO and EtBr dyes. However, the presence of green colour in living cells indicates that they are only permeable to AO.[58] Following the seeding process, 3 T3 cells attach to the scaffolds by acquiring a spherical shape, as seen in Fig. 8. When 3 T3 cells are cultured further, they spread out further across the surface of the scaffold and start to proliferate. The results indicate that 3 T3 cells attach and proliferate in a comparable manner on PLA and PLA/C scaffolds, but show significantly improved adherence and proliferation on the PLA/CNLC scaffold. The MTT test results of 3 T3 cells cultured on the scaffold support these findings, indicating that the inclusion of CNLC significantly impacts the biological suitability of the 3D bioprinted scaffold.

3.13 *In vivo* wound healing assay

The wound healing ability of the 3D bioprinted PLA, PLA/C, and PLA/CNLC scaffolds was assessed by analysing wound regions and assessing wound closure. The scaffolds exhibited strong adherence to the wound site in all the three groups during surgery, and none of them had any post-operative problems such as infection or swelling. Fig. 9(a and b) demonstrates the efficacy of scaffolds in promoting wound healing in an excision model. On the 7th, 14th, 21st, and 28th days after the injury, there was a decrease in the size of the wound. Fig. 9(b) demonstrates that the healing of wounds in the PLA/CNLC sample group was significantly better than that in the PLA and PLA/C groups, as seen in comparison with the control group. On the seventh day, the percentage of wound closure was around 42% for the PLA/CNLC group, 41 ± 2.6% for the PLA/C group, 26% for the blank PLA group, and 18% for the control group. By day 21, the wounds had fully healed for PLA/CNLC, with a closure rate of 70%. For PLA/C, the closure rate was 48%. The closure rates for blank PLA and the control group were 44% and 31% respectively. On day 21, the effectiveness of PLA/CNLC scaffolds in wound healing demonstrated complete closure of the wound. Fig. 9(a) displays photos of injuries incurred by each group.

3.14 Biochemical assessment

Various binding proteins play a crucial role in the skin's reaction throughout the process of wound healing. Inflammation cells play a role in promoting the growth of endothelial cells during the healing process, which in turn supports the development of new blood vessels, creation of collagen, and restoration of damaged regions with new epithelial cells. Matrix constituents such as hydroxyproline and hexosamine play a role in the creation of fresh extracellular matrix. Connective tissue scleroproteins, such as collagen and elastin, are composed of the amino acid hydroxyproline. Hydroxyproline has shown to be a dependable indicator for identifying the presence of collagen and monitoring its metabolic processes. Hexosamine, a matrix molecule, serves as a fundamental component for the creation of fresh extracellular matrix. It promotes the synthesis of extracellular matrix, hence facilitating wound healing *via* the upregulation of hyaluronic acid production. Prior studies have shown that an elevation in the concentration of these molecules facilitates the process of tissue healing after an injury.[59] The concentrations of hydroxyproline and hexosamine in the granulation tissue were assessed on the zeroth and 14th day in the groups of rats undergoing therapy. Fig. 10 shows the efficacy of scaffolds in influencing hydroxyproline and hexosamine levels. On the 14th day, the amounts of hydroxyproline (12.64 ± 1.2 mg g^{-1}) and hexosamine (10.21 ± 1.92 mg g^{-1}) were significantly higher in the 3D bioprinted PLA/CNLC group compared to the control group. This suggests that there was an enhanced deposition of collagen in the 3D bioprinted PLA/CNLC group. The efficacy of 3D bioprinted PLA/C in restoring hydroxyproline (4.73 ± 0.68 mg g^{-1}) and hexosamine (3.2 ± 0.63 mg g^{-1}) levels in mice was reduced on day 14. The presence of higher levels of collagen at the wound site serves as a clear indication of the quantity of fibroblasts that are actively depositing new tissue, suggesting an early phase in the healing process. The presence of greater amounts of hydroxyproline and hexosamine compounds in PLA/CNLC scaffolds, as compared to PLA/C scaffolds, confirms the better capability of CNLC in promoting wound healing.

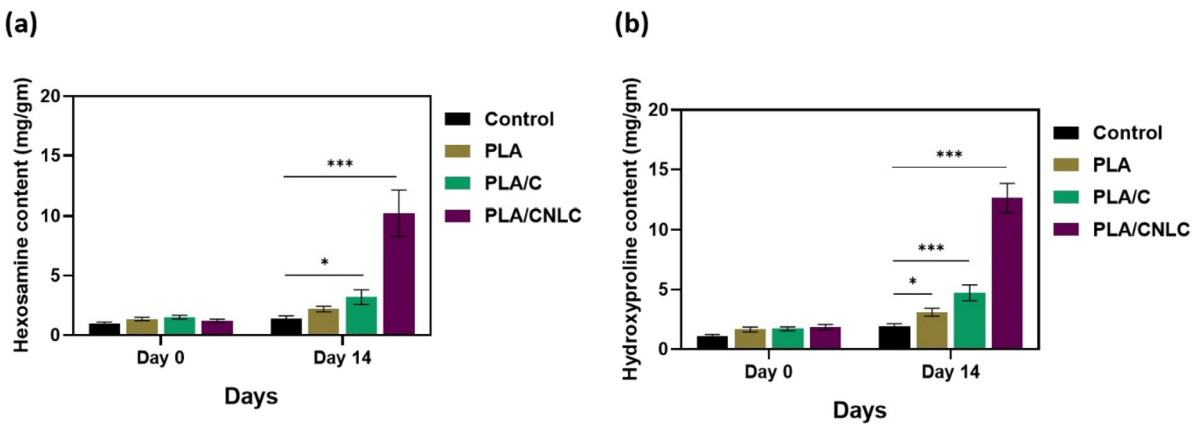

Fig. 10 Impact of 3D bioprinted scaffolds on (a) the hydroxyproline content and (b) the hexosamine content of rats on the zeroth and 14th day post wounding.

3.15 Histological analysis

In order to assess the efficacy of the 3D bioprinted PLA, PLA/C, and PLA/CNLC scaffolds in promoting wound healing and skin reconstruction, the skin tissues were subjected to haematoxylin & eosin staining. The findings demonstrated that the levels of epithelialisation, maturation, and tissue regeneration were enhanced throughout the process of wound healing after 4 weeks of surgery (Fig. 11). The 3D bioprinted PLA/CNLC shows the development of granulation tissue on the surface on day 7, which was then followed by the production of a thin, intermittent layer of squamous epithelium on day 14. Ultimately, the whole incision region became completely covered by newly formed tissue on day 21. There was a significant increase in the growth and development of outer skin cells, along with a large number of fibroblasts, excessive growth of granulation tissue, and dense deposition of collagen. After 2 weeks of the surgery, the 3D bioprinted PLA/C group showed the development of granulation tissue in the wound, along with the initiation of movement by the epithelial cells. After 3 weeks, a delicate layer of epithelial tissue developed on the surface of the wound. The wound healing of the untreated control group and the PLA group was delayed in comparison with the PLA/C and PLA/CNLC groups. The process of wound healing was seen to progress from the periphery towards the centre after 4 weeks. Nevertheless, the central portions of the wound were only partially covered by the outermost layer of skin, known as the epidermis. An uneven layer of the thinner outer skin had developed. The dermis of wounds in the 3D bioprinted PLA/CNLC group exhibited a higher level of maturity compared to the control group. The results consistently showed that the wounds treated with 3D bioprinted PLA/CNLC exhibited superior healing compared to all the other groups.

4. Conclusion

The study successfully developed curcumin-loaded nanostructured lipid carriers (CNLC) and integrated them into PLA and fabricated 3D bioprinted scaffolds. A melt dispersion ultrasonication technique was used to develop CNLC and they exhibited a narrow particle size distribution (200–500 nm), high entrapment efficiency (81.37 ± 0.85%), and satisfactory drug loading capacity (6.59 ± 1.61%). Rheological analysis confirmed the suitability of bioinks for 3D printing, demonstrating shear-thinning behaviour and appropriate viscosity. The 3D constructs of PLA, PLA/C, and PLA/CNLC scaffolds were created using a pneumatic extrusion-based 3D printing approach. FTIR characterization of the 3D-printed scaffolds revealed the presence of functional groups indicating successful incorporation of CNLC into the PLA matrix. The scanning

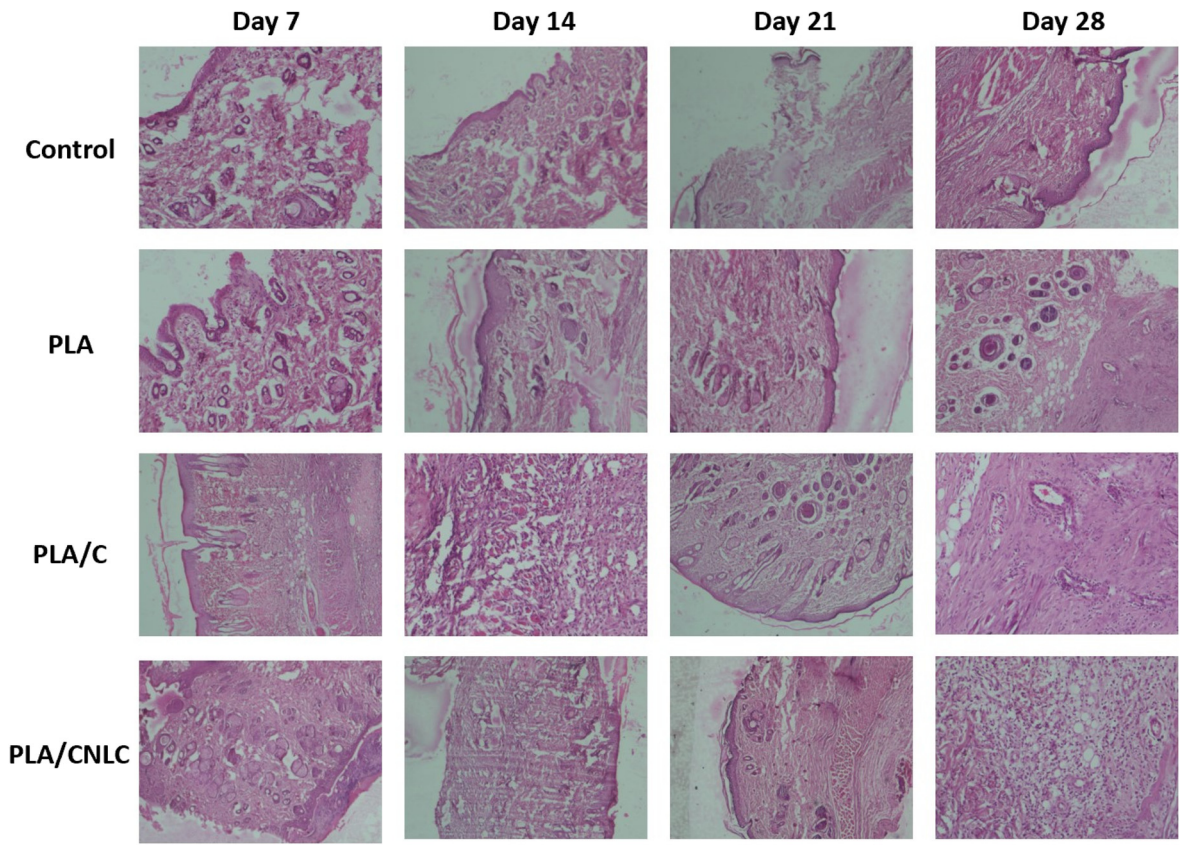

Fig. 11 Histological images of the granulation tissue after gauze, 3D bioprinted PLA, PLA/C, and PLA/CNLC therapy, as shown in the haematoxylin and eosin-stained section.

electron microscopy (SEM) study of the scaffolds revealed the presence of uninterrupted filament development and ideal porosity (200 μm). The antibacterial assay demonstrated that PLA/CNLC had strong antimicrobial capabilities against *Escherichia coli* and *Staphylococcus aureus*, effectively lowering the bacterial population. *In vitro* studies demonstrated that the PLA/CNLC scaffolds supported cell proliferation and were non-cytotoxic. *In vivo* experiments on rats confirmed the efficacy of the scaffolds in promoting wound healing, with complete wound closure being observed within 21 days. Overall, the integration of CNLC into 3D-printed PLA scaffolds presents a promising approach for enhancing wound healing and advancing regenerative medicine applications. While the study demonstrates promising results, several limitations must be acknowledged, particularly regarding the translation of 3D bioprinting technology to clinical applications. Scaling up 3D bioprinting for large-scale production presents significant challenges, including maintaining uniform scaffold properties, managing high production costs, and ensuring regulatory compliance. Variability in scaffold porosity, mechanical strength, and therapeutic agent distribution could impact the reproducibility and efficacy of scaffolds on a clinical scale. Addressing these challenges will require further research into scalable manufacturing techniques, and comprehensive long-term *in vivo* studies to ensure safety and efficacy in clinical settings.

Author contributions

Ms Renuka Vijayaraghavan was involved in experiments, characterization, data collection, formal analysis, validation and preparation of the original draft. Dr M. Vidyavathi, Dr Sravanthi Loganathan and Dr Ravi Babu Valapa were involved in acquiring resources and provided equal contribution in conceptualization, development of methodology, characterization, formal analysis, validation, write-up, and review & editing. All of them were involved in supervision of the work and funding acquisition.

Data availability

Data will be made available on request.

Conflicts of interest

The authors declare that they have no known competing financial interests or personal relationships that could have appeared to influence the work reported in this paper.

Acknowledgements

Dr Sravanthi Loganathan thanks the Department of Science and Technology, Government of India, for supporting this research through the DST INSPIRE FACULTY Scheme (Grant No. DST/INSPIRE/04/2017/000704) and the Director, Central Electrochemical Research Institute (CECRI). Dr Ravi Babu Valapa thanks the Director, CSIR-CECRI for supporting this research under the "In-house" project plan (Grant no. IHP 0148). The Central Instrument Facility (CIF) at CSIR-CECRI is acknowledged on behalf of the authors for providing characterisation tools including FE-SEM, AFM, XRD, FTIR, DSC, and TGA. The CSIR-CECRI is appreciated by all the authors for providing the 3D bioprinting facility. Ms Renuka Vijayaraghavan expresses gratitude to CSIR-HQ, New Delhi for the GATE-Junior Research Fellowship grant (JRF).

References

1 A. Ehterami, M. Salehi, S. Farzamfar, H. Samadian, A. Vaez, H. Sahrapeyma, *et al.*, A promising wound dressing based on alginate hydrogels containing vitamin D3 cross-linked by calcium carbonate/d-glucono-δ-lactone, *Biomed. Eng. Lett.*, 2020, **10**(2), 309–319.
2 P. Victor, D. Sarada and K. M. Ramkumar, Pharmacological activation of Nrf2 promotes wound healing, *Eur. J. Pharmacol.*, 2020, **886**, 173395.
3 D. Simões, S. P. Miguel, M. P. Ribeiro, P. Coutinho, A. G. Mendonça and I. J. Correia, Recent advances on antimicrobial wound dressing: A review, *Eur. J. Pharm. Biopharm.*, 2018, **127**, 130–141.
4 R. Augustine, S. R. U. Rehman, R. Ahmed, A. A. Zahid, M. Sharifi, M. Falahati, *et al.*, Electrospun chitosan membranes containing bioactive and therapeutic agents for enhanced wound healing, *Int. J. Biol. Macromol.*, 2020, **156**, 153–170.
5 M. B. Dreifke, A. A. Jayasuriya and A. C. Jayasuriya, Current wound healing procedures and potential care, *Mater. Sci. Eng., C*, 2015, **48**, 651–662.
6 P. Mohd and A. Zahra, Alginate/Gauze Incorporated with Hibiscus sabdariffa Linn. Extract as a Bioactive Agent for Wound Dressing Application, *JOMALISC*, 2023, 105–114.
7 K. E. Milne and J. G. Penn-Barwell, Classification and management of acute wounds and open fractures, *Surgery*, 2020, **38**(3), 143–149.
8 N. Zainuddin, I. Ahmad, M. H. Zulfakar, H. Kargarzadeh and S. Ramli, Cetyltrimethylammonium bromide-nanocrystalline cellulose (CTAB-NCC) based microemulsions for enhancement of topical delivery of curcumin, *Carbohydr. Polym.*, 2021, **254**, 117401.
9 T. K. Hunt, M. Linsey, G. Crislis, M. Sonne and E. Jawetz, The Effect of Differing Ambient Oxygen Tensions on Wound Infection, *Ann. Surg.*, 1975, **181**(1), 35–39.
10 M. C. Robson, B. D. Stenberg and J. P. Heggers, Wound Healing Alterations Caused by Infection, *Clin. Plast. Surg.*, 1990, **17**(3), 485–492.
11 E. Engelhardt, A. Toksoy, M. Goebeler, S. Debus, E. B. Bröcker and R. Gillitzer, Chemokines IL-8, GROα, MCP-1, IP-10, and Mig Are Sequentially and Differentially

Expressed During Phase-Specific Infiltration of Leukocyte Subsets in Human Wound Healing, *Am. J. Pathol.*, 1998, **153**(6), 1849–1860.
12 C. H. Thomson, Biofilms: do they affect wound healing?, *Int. Wound J.*, 2010, **8**(1), 63–67.
13 C. K. Sen, Human Wounds and Its Burden: An Updated Compendium of Estimates, *Adv. Wound Care.*, 2019, **8**(2), 39–48.
14 A. Majumdar and P. N. Sangole, *Alternative Approaches to Wound Healing*, 2016.
15 Z. Rafiee, M. Nejatian, M. Daeihamed and S. M. Jafari, Application of curcumin-loaded nanocarriers for food, drug and cosmetic purposes, *Trends Food Sci. Technol.*, 2019, **88**, 445–458.
16 B. Salehi, Z. Stojanović-Radić, J. Matejić, M. Sharifi-Rad, N. V. Anil Kumar, N. Martins, *et al.*, The therapeutic potential of curcumin: A review of clinical trials, *Eur. J. Med. Chem.*, 2019, **163**, 527–545.
17 T. Jiang, W. Liao and C. Charcosset, Recent advances in encapsulation of curcumin in nanoemulsions: A review of encapsulation technologies, bioaccessibility and applications, *Food Res. Int.*, 2020, **132**, 109035.
18 S. C. Gupta, S. Prasad, J. H. Kim, S. Patchva, L. J. Webb, I. K. Priyadarsini, *et al.*, Multitargeting by curcumin as revealed by molecular interaction studies, *Nat. Prod. Rep.*, 2011, **28**(12), 1937.
19 K. Priyadarsini, The Chemistry of Curcumin: From Extraction to Therapeutic Agent, *Molecules*, 2014, **19**(12), 20091–20112.
20 A. Barzegar and A. A. Moosavi-Movahedi, Intracellular ROS Protection Efficiency and Free Radical-Scavenging Activity of Curcumin, *PLoS One*, 2011, **6**(10), e26012.
21 A. Shehzad and Y. S. Lee, Molecular mechanisms of curcumin action: Signal transduction, *BioFactors*, 2013, **39**(1), 27–36.
22 Y. He, Y. Yue, X. Zheng, K. Zhang, C. S. Du and Z. Curcumin, Inflammation, and Chronic Diseases: How Are They Linked?, *Molecules*, 2015, **20**(5), 9183–9213.
23 Y. Panahi, O. Fazlolahzadeh, S. L. Atkin, M. Majeed, A. E. Butler, T. P. Johnston, *et al.*, Evidence of curcumin and curcumin analogue effects in skin diseases: A narrative review, *J. Cell. Physiol.*, 2018, **234**(2), 1165–1178.
24 M. Bhatia and M. Saini, Formulation and evaluation of curcumin microsponges for oral and topical drug delivery, *Prog. Biomater.*, 2018, **7**(3), 239–248.
25 L. Sun, Z. Liu, L. Wang, D. Cun, H. H. Y. Tong, R. Yan, X. Chen, R. Wang and Y. Zheng, Enhanced topical penetration, system exposure and anti-psoriasis activity of two particle-sized, curcumin-loaded PLGA nanoparticles in hydrogel, *J. Controlled Release*, 2017, **254**, 44–54.
26 Z. Terzopoulou, A. Michopoulou, A. Palamidi, E. Koliakou and D. Bikiaris, Preparation and Evaluation of Collagen-Based Patches as Curcumin Carriers, *Polymers*, 2020, **12**(10), 2393.
27 N. Fereydouni, M. Darroudi, J. Movaffagh, A. Shahroodi, A. E. Butler, S. Ganjali, *et al.*, Curcumin nanofibers for the purpose of wound healing, *J. Cell. Physiol.*, 2018, **28**, 5537–5554.
28 M. K. Jeengar, S. V. K. Rompicharla, S. Shrivastava, N. Chella, N. R. Shastri, V. G. M. Naidu, *et al.*, Emu oil based nano-emulgel for topical delivery of curcumin, *Int. J. Pharm.*, 2016, **506**(1–2), 222–236.
29 V. K. Rapalli, V. Kaul, T. Waghule, S. Gorantla, S. Sharma, A. Roy, *et al.*, Curcumin loaded nanostructured lipid carriers for enhanced skin retained topical delivery: optimization, scale-up, *in vitro* characterization and assessment of *ex vivo* skin deposition, *Eur. J. Pharm. Sci.*, 2020, **152**, 105438.
30 Y. Agrawal, K. C. Petkar and K. K. Sawant, Development, evaluation and clinical studies of Acitretin loaded nanostructured lipid carriers for topical treatment of psoriasis, *Int. J. Pharm.*, 2010, **401**(1–2), 93–102.
31 H. Lee, G. Han, Y. Na, M. Kang, S. Bang, H. S. Kang, *et al.*, 3D–Printed Tissue–Specific Nanospike–Based Adhesive Materials for Time–Regulated Synergistic Tumor Therapy and Tissue Regeneration In Vivo, *Adv. Funct. Mater.*, 2024, **34**(48), 2406237.
32 G. Han, H. Lee, J. M. Kang, J. H. Park, E. Lee, E. S. Lee, *et al.*, 3D-printed NIR-responsive bullets as multifunctional nanodrug platforms for image-guided local chemo-photothermal therapy, *Chem. Eng. J.*, 2023, **477**, 147083–147083.
33 P. Gunatillake, Biodegradable synthetic polymers for tissue engineering, *Eur. Cells Mater.*, 2003, **5**, 1–16.
34 F. I. Butt, N. Muhammad, A. Hamid, M. Moniruzzaman and F. Sharif, Recent progress in the utilization of biosynthesized polyhydroxyalkanoates for biomedical applications – Review, *Int. J. Biol. Macromol.*, 2018, **120**, 1294–1305.
35 B. Jia, H. Huang, Z. Dong, X. Ren, Y. Lu, W. Wang, *et al.*, Degradable biomedical elastomers: paving the future of tissue repair and regenerative medicine, *Chem. Soc. Rev.*, 2024, **53**(8), 4086–4153.
36 S. Zhang, H. Fang and H. Tian, Recent Advances in Degradable Biomedical Polymers for Prevention, Diagnosis and Treatment of Diseases, *Biomacromolecules*, 2024, **25**(11), 7015–7057.
37 M. U. A. Khan, M. A. Aslam, M. F. Abdullah, A. Hasan, S. A. Shah and G. M. Stojanović, Recent perspective of polymeric biomaterial in tissue engineering– a review, *Mater. Today Chem.*, 2023, **34**, 101818–101818.
38 M. Cui, L. Liu, N. Guo, R. Su and F. Ma, Preparation, cell compatibility and degradability of collagen-modified poly (lactic acid), *Molecules*, 2015, **20**(1), 595–607.
39 I. Jazuli, Annu, B. Nabi, T. Moolakkadath, T. Alam, S. Baboota, *et al.*, Optimization of Nanostructured Lipid Carriers of Lurasidone Hydrochloride Using Box-Behnken Design for Brain Targeting: In Vitro and In Vivo Studies, *J. Pharm. Sci.*, 2019, **108**(9), 3082–3090.
40 M. Kumar, A. Tiwari, S. M. B. Asdaq, A. B. Nair, S. Bhatt, P. Shinu, *et al.*, Itraconazole loaded nano-structured lipid carrier for topical ocular delivery: Optimization and evaluation, *Saudi J. Biol. Sci.*, 2022, **29**(1), 1–10.
41 M. Ganeshkumar, T. Ponrasu, R. Krithika, K. Iyappan, V. S. Gayathri and L. Suguna, Topical application of

Acalypha indica accelerates rat cutaneous wound healing by up-regulating the expression of Type I and III collagen, *J. Ethnopharmacol.*, 2012, **142**(1), 14–22.

42 S. Barua and S. Mitragotri, Challenges associated with Penetration of Nanoparticles across Cell and Tissue Barriers: A Review of Current Status and Future Prospects, *Nano Today*, 2014, **9**(2), 223–243.

43 D. Bhalani, B. Nutan, A. Kumar and A. K. Singh Chandel, Bioavailability Enhancement Techniques for Poorly Aqueous Soluble Drugs and Therapeutics, *Biomedicines*, 2022, **10**(9), 2055.

44 D. Khater, H. Nsairat, F. Odeh, M. Saleh, A. Jaber, W. Alshaer, *et al.*, Design, Preparation, and Characterization of Effective Dermal and Transdermal Lipid Nanoparticles: A Review, *Cosmetics*, 2021, **8**(2), 39.

45 D. Zhang, Q. Fu, H. Fu, J. Zeng, L. Jia and M. Chen, 3D-bioprinted human lipoaspirate-derived cell-laden skin constructs for healing of full-thickness skin defects, *Int. J. Bioprint.*, 2023, **9**(4), 718.

46 E. H. Ismail, D. Y. Sabry, H. Mahdy and M. M. H. Khalil, Synthesis and Characterization of some Ternary Metal Complexes of Curcumin with 1,10-phenanthroline and their Anticancer Applications, *J. Sci. Res.*, 2014, **6**(3), 509–519.

47 V. S. Chaudhari, U. S. Murty and S. Banerjee, Nanostructured lipid carriers as a strategy for encapsulation of active plant constituents: Formulation and in vitro physicochemical characterizations, *Chem. Phys. Lipids*, 2021, **235**, 105037–105037.

48 G. Karthikeyan, M. K. Swamy, M. R. Viknesh, R. Shurya and N. Sudhakar, *Bioactive Phytocompounds to Fight Against Antimicrobial Resistance*, Springer eBooks, 2020, pp. 335–381.

49 M. T. Bayode, E. F. Awodire, E. F. Ojo, G. O. Adenikinju, M. E. Sadibo, P. O. Aro, *et al.*, Phytophenolic derivatives as potential ameliorative agents for microbial superbugs: mechanisms of action, cellular pathways and synergistic selectivity with chemotherapeutics, *Discover Appl. Sci.*, 2024, **6**(9), 484.

50 Prateeksha, C. V. Rao, A. K. Das, S. K. Barik and B. N. Singh, ZnO/Curcumin Nanocomposites for Enhanced Inhibition of Pseudomonas aeruginosa Virulence via LasR-RhlR Quorum Sensing Systems, *Mol. Pharm.*, 2019, **16**(8), 3399–3413.

51 J. Chadha, K. Harjai and S. Chhibber, Repurposing phytochemicals as anti–virulent agents to attenuate quorum sensing–regulated virulence factors and biofilm formation in Pseudomonas aeruginosa, *Microb. Biotechnol.*, 2021, **15**(6), 1695–1718.

52 J. Liu, X. Han, T. Zhang, K. Tian, Z. Li and F. Luo, Reactive oxygen species (ROS) scavenging biomaterials for anti-inflammatory diseases: from mechanism to therapy, *J. Hematol. Oncol.*, 2023, **16**(1), 116.

53 C. F. Lima, C. Pereira-Wilson and S. I. S. Rattan, Curcumin induces heme oxygenase-1 in normal human skin fibroblasts through redox signaling: Relevance for anti-aging intervention, *Mol. Nutr. Food Res.*, 2010, **55**(3), 430–442.

54 J. Wu, F. Ibtisham, Y. F. Niu, Z. Wang, G. H. Li, Y. Zhao, *et al.*, Curcumin inhibits heat-induced oxidative stress by activating the MAPK-Nrf2/ARE signaling pathway in chicken fibroblasts cells, *J. Therm. Biol.*, 2019, **79**, 112–119.

55 The Molecular Targets and Therapeutic Uses of Curcumin in Health and Disease, *Advances In Experimental Medicine And Biology*. ed. B. B. Aggarwal, Y. J. Surh and S. Shishodia, Springer US, Boston, MA, 2007.

56 X. Dai, J. Liu, H. Zheng, J. Wichmann, U. Hopfner, S. Sudhop, *et al.*, Nano-formulated curcumin accelerates acute wound healing through Dkk-1-mediated fibroblast mobilization and MCP-1-mediated anti-inflammation, *NPG Asia Mater.*, 2017, **9**(3), e368–e368.

57 M. Ashrafizadeh, A. Zarrabi, K. Hushmandi, V. Zarrin, E. R. Moghadam, F. Hashemi, *et al.*, Toward Regulatory Effects of Curcumin on Transforming Growth Factor-Beta Across Different Diseases: A Review, *Front. Pharmacol.*, 2020, **11**, 585413.

58 S. Kari, K. Subramanian, I. A. Altomonte, A. Murugesan, O. Yli-Harja and M. Kandhavelu, Programmed cell death detection methods: a systematic review and a categorical comparison, *Apoptosis*, 2022, **27**(7–8), 482–508.

59 M. Rodrigues, N. Kosaric, C. A. Bonham and G. C. Gurtner, Wound Healing: A Cellular Perspective, *Physiol. Rev.*, 2018, **99**(1), 665–706.